Sparse identification of a predator-prey system from simulation data of a convection model

Dam, Magnus; Brøns, Morten; Rasmussen, Jens Juul; Naulin, Volker; Hesthaven, Jan S.

Published in:
Physics of Plasmas

Link to article, DOI:
10.1063/1.4977057

Publication date:
2017

Document Version
Publisher's PDF, also known as Version of record

Sparse identification of a predator-prey system from simulation data of a convection model

Magnus Dam, Morten Brøns, Jens Juul Rasmussen, Volker Naulin, and Jan S. Hesthaven

Citation: Physics of Plasmas **24**, 022310 (2017); doi: 10.1063/1.4977057
View online: http://dx.doi.org/10.1063/1.4977057
View Table of Contents: http://aip.scitation.org/toc/php/24/2
Published by the American Institute of Physics

Sparse identification of a predator-prey system from simulation data of a convection model

Magnus Dam,[1] Morten Brøns,[1] Jens Juul Rasmussen,[2] Volker Naulin,[2] and Jan S. Hesthaven[3]
[1]*Department of Applied Mathematics and Computer Science, Technical University of Denmark, DK-2800 Kgs. Lyngby, Denmark*
[2]*Department of Physics, Technical University of Denmark, DK-2800 Kgs. Lyngby, Denmark*
[3]*Mathematics Institute of Computational Science and Engineering, École Polytechnique Fédérale de Lausanne, CH-1015 Lausanne, Switzerland*

(Received 7 December 2016; accepted 8 February 2017; published online 28 February 2017)

The use of low-dimensional dynamical systems as reduced models for plasma dynamics is useful as solving an initial value problem requires much less computational resources than fluid simulations. We utilize a data-driven modeling approach to identify a reduced model from simulation data of a convection problem. A convection model with a pressure source centered at the inner boundary models the edge dynamics of a magnetically confined plasma. The convection problem undergoes a sequence of bifurcations as the strength of the pressure source increases. The time evolution of the energies of the pressure profile, the turbulent flow, and the zonal flow capture the fundamental dynamic behavior of the full system. By applying the sparse identification of nonlinear dynamics (SINDy) method, we identify a predator-prey type dynamical system that approximates the underlying dynamics of the three energy state variables. A bifurcation analysis of the system reveals consistency between the bifurcation structures, observed for the simulation data, and the identified underlying system. *Published by AIP Publishing*. [http://dx.doi.org/10.1063/1.4977057]

I. INTRODUCTION

The perpendicular edge transport of a magnetically confined plasma is largely governed by convective plasma flows. The plasma flows can be decomposed into a non-zonal (turbulent, fluctuating) flow and a zonal flow. The non-zonal flow increases the radial transport and generates a Reynolds stress that drives the zonal flow. The zonal flow is in the poloidal direction along the magnetic flux surfaces and varies radially. This sheared poloidal flow constitutes a transport barrier that decreases the radial transport of plasma. While the zonal flow is turbulence-driven, it also suppresses the turbulent flow. This type of interaction between the turbulent energy and the zonal flow energy resembles mathematically the interaction between populations of predators and preys. The interaction between turbulent flow and zonal flow has therefore been modeled by predator-prey systems, where the zonal flow acts as the predator and the turbulent flow acts as the prey.[1,2] The creation of an edge transport barrier formed by a sheared zonal flow is closely related to the L–H transition.[3] Ordinary differential equation (ODE) models for the L–H transition are based on the predator-prey relationship between zonal flow and turbulent flow, and incorporate a potential energy related to the pressure profile as an additional state variable.[4–12] Miki *et al.*[13] and Wu *et al.*[14] have both suggested 1D partial differential equation (PDE) models for the L–H transition based on this predator-prey relationship.

Reduced ODE models, describing the interaction between zonal flow and turbulent flow, are very useful. ODE models require much less computational resources to solve and they are much easier to analyze than the corresponding fluid equations. When building a mathematical model, there are basically two different approaches to choose among. The first one is physical modeling, where the model is derived from theory. The second approach is system identification,[15] where observed data from the real system are used to model the system. System identification is a large and diverse field and many methods exist for determining the governing equations of a system from data. The choice of an identification method depends on the desired model type, prior knowledge about the model structure, and other model assumptions.

Most current predator-prey models for the interaction between zonal flow and turbulent flow are obtained by physical modeling with many approximations and assumptions. The Ball-Dewar-Sugama model[5] is loosely derived from approximate resistive magnetohydrodynamics momentum and pressure convection equations, and the Kim-Diamond model[6] is loosely derived from the linearized wave-kinetic equation. Even though these models reproduce qualitative dynamics similar to experimental observations, they fail to be quantitatively predictive. Kobayashi, Güurcan, and Diamond[16] use an identification approach, where they assume that a Lotka-Volterra model describes the interaction between zonal flow and turbulent flow, and fit the model coefficients to data obtained from full gyrokinetic simulations. However, this simple model fails to describe the dynamics away from the limit cycle attractor.

This paper demonstrates an alternative approach for building ODE models for plasma dynamics. We extract a model from data instead of obtaining the model using physics-based arguments. Specifically, we determine the underlying structure of a nonlinear dynamical system from simulations of a

convection problem with a pressure source centered at the left boundary. The convection problem undergoes a sequence of transitions as the strength of the pressure source increases. These transitions are similar to the ones observed in more accurate plasma models. The time evolution of the energies of the pressure profile, the turbulent flow, and the zonal flow capture the bifurcating behavior of the full convection problem. We model these three energy state variables with a continuous deterministic dynamical system and assume no prior knowledge about the structure of the dynamical system. For the system identification process, we apply the sparse identification of nonlinear dynamics (SINDy) method[17] and aim to build a model that quantitatively reproduces the dynamics and bifurcations observed in the simulation data. The method is general enough that the same approach can be used if the simulation data were replaced by measurement data.

II. SPARSE IDENTIFICATION OF NONLINEAR DYNAMICS (SINDy)

SINDy[17] is a method that seeks to identify an underlying dynamical system from time-series data. We give here a brief summary of the algorithm description. Based on a set of data, we seek a dynamical system

$$\dot{\boldsymbol{x}} = \boldsymbol{f}(\boldsymbol{x}), \quad \boldsymbol{x} \in \mathbb{R}^n. \tag{1}$$

Here, $\boldsymbol{x}(t) = [\,x_1(t) \quad x_2(t) \quad \cdots \quad x_n(t)\,]^\top$ is the state variable vector and $\boldsymbol{f} = [\,f_1(x) \quad f_2(x) \quad \cdots \quad f_n(x)\,]^\top$ is the vector field. We want to determine the function $\boldsymbol{f}$ from data. In the data-collection process, we sample a time-series of the state $\boldsymbol{x}(t)$ and either measure the derivative $\dot{\boldsymbol{x}}(t)$ or approximate it numerically from the time-series of $\boldsymbol{x}(t)$. The data $\boldsymbol{x}(t_\ell)$ and $\dot{\boldsymbol{x}}(t_\ell)$, $\ell = 1, \ldots, m$ are arranged into two matrices

$$\boldsymbol{X} = \begin{bmatrix} \boldsymbol{x}^\top(t_1) \\ \boldsymbol{x}^\top(t_2) \\ \vdots \\ \boldsymbol{x}^\top(t_m) \end{bmatrix} = \begin{bmatrix} x_1(t_1) & x_2(t_1) & \cdots & x_n(t_1) \\ x_1(t_2) & x_2(t_2) & \cdots & x_n(t_2) \\ \vdots & \vdots & \ddots & \vdots \\ x_1(t_m) & x_2(t_m) & \cdots & x_n(t_m) \end{bmatrix},$$

$$\dot{\boldsymbol{X}} = \begin{bmatrix} \dot{\boldsymbol{x}}^\top(t_1) \\ \dot{\boldsymbol{x}}^\top(t_2) \\ \vdots \\ \dot{\boldsymbol{x}}^\top(t_m) \end{bmatrix} = \begin{bmatrix} \dot{x}_1(t_1) & \dot{x}_2(t_1) & \cdots & \dot{x}_n(t_1) \\ \dot{x}_1(t_2) & \dot{x}_2(t_2) & \cdots & \dot{x}_n(t_2) \\ \vdots & \vdots & \ddots & \vdots \\ \dot{x}_1(t_m) & \dot{x}_2(t_m) & \cdots & \dot{x}_n(t_m) \end{bmatrix}.$$

We construct an augmented library $\Theta(\boldsymbol{X})$ consisting of candidate functions of the columns of $\boldsymbol{X}$. The candidate functions could be a constant, polynomials, trigonometric terms, etc. Here, we will be using polynomial terms as candidate functions

$$\Theta(\boldsymbol{X}) = \begin{bmatrix} 1 & \boldsymbol{X} & \boldsymbol{X}^{P_2} & \boldsymbol{X}^{P_3} & \cdots \end{bmatrix},$$

where $\boldsymbol{X}^{P_i}$ are ith order polynomials of $\boldsymbol{X}$. Each column of $\Theta(\boldsymbol{X})$ represents a candidate function for the vectorfield $\boldsymbol{f}(\boldsymbol{x})$. We assume that only a few of these terms are active in each row of $\boldsymbol{f}(\boldsymbol{x})$. We can then write $\boldsymbol{f}(\boldsymbol{X}) = \Theta(\boldsymbol{X})\Xi$, where $\Xi = [\,\boldsymbol{\xi}_1 \quad \boldsymbol{\xi}_2 \quad \cdots \quad \boldsymbol{\xi}_n\,]$ is a sparse matrix of coefficients. The coefficient matrix Ξ can be determined from the sparse regression problem

$$\dot{\boldsymbol{X}} = \Theta(\boldsymbol{X})\Xi. \tag{2}$$

Each column $\boldsymbol{\xi}_k$ of Ξ is a sparse vector of coefficients and determines which terms are active in the right-hand side of the corresponding row equation $\dot{x}_k = f_k(\boldsymbol{x})$ in (1). Once Ξ has been determined, each row of $\boldsymbol{f}$ may be determined by

$$\dot{x}_k = f_k(\boldsymbol{x}) = \Theta(\boldsymbol{x}^\top)\boldsymbol{\xi}_k, \quad k = 1, \ldots, n.$$

To solve for Ξ in (2), we implement the algorithm described in Ref. 17. Let $\Theta(\boldsymbol{X})$ have dimensions $m \times p$, where p is the number of candidate functions and m is the number of time samples. We assume $m \gg p$ since there are many more time samples of data than there are candidate functions. Since both $\boldsymbol{X}$ and $\dot{\boldsymbol{X}}$ are generally contaminated with noise, (2) does not hold exactly. Instead

$$\dot{\boldsymbol{X}} = \Theta(\boldsymbol{X})\Xi + \eta\boldsymbol{Z}, \tag{3}$$

where $\boldsymbol{Z}$ is a matrix of independent identically distributed Gaussian entries with zero mean, and η is the noise magnitude. We seek to solve for Ξ in (3). To ensure that the restricted isometry property holds, we normalize the columns of $\Theta(\boldsymbol{X})$ to a length of 1 by dividing each column by the ℓ^2-norm of that column.[18] Let $\boldsymbol{l}_2$ denote the vector of ℓ^2-norms of the columns of $\Theta(\boldsymbol{X})$. We use that $\mathrm{diag}(1/\boldsymbol{l}_2) = [\mathrm{diag}(\boldsymbol{l}_2)]^{-1}$ to define a scaled coefficient matrix such that the structure of (3) is unchanged

$$\Theta(\boldsymbol{X})\Xi = \underbrace{\Theta(\boldsymbol{X})\mathrm{diag}(1/\boldsymbol{l}_2)}_{\Theta_{\mathrm{sc}}(\boldsymbol{X})}\underbrace{\mathrm{diag}(\boldsymbol{l}_2)\Xi}_{\Xi_{\mathrm{sc}}} = \Theta_{\mathrm{sc}}(\boldsymbol{X})\Xi_{\mathrm{sc}}.$$

In the algorithm, Ξ_{sc} is initialized as the least-squares solution. In each column of Ξ_{sc}, all elements in the coefficient vector $\boldsymbol{\xi}_{k,\mathrm{sc}}$, smaller than a threshold value λ_k, are set to zero. Then, a new least-squares solution for Ξ_{sc} is obtained for the remaining non-zero indices. These new coefficients are again set to zero if they are smaller than their column's threshold value, λ_k, and the procedure is continued until the non-zero elements of Ξ_{sc} converge. Finally, the non-normalized coefficient matrix is given by $\Xi = \mathrm{diag}(1/\boldsymbol{l}_2)\Xi_{\mathrm{sc}}$.

The algorithm is easily adjusted to include dependence on a parameter, i.e., to consider systems on the form $\dot{\boldsymbol{x}} = \boldsymbol{f}(\boldsymbol{x}; \mu)$. The parameter μ is simply treated as an additional state variable with zero time derivative in the algorithm. The identification must then be based on a collection of time series of the state variables obtained for multiple fixed values of the parameter. The algorithm also allows time-dependence and external forcing of the vector field, i.e., systems on the form $\dot{\boldsymbol{x}} = \boldsymbol{f}(\boldsymbol{x}, \boldsymbol{u}(t), t)$. Here, the time variable t and the external forcing $\boldsymbol{u}(t)$ are just added in the algorithm as additional variables.

III. SIMULATION DATA GENERATION

We consider viscous plasma flow in a rectangular domain at the edge of a magnetically confined plasma in the

plane perpendicular to the magnetic field $\boldsymbol{B} = B_0 \boldsymbol{e}_z$. The transport of plasma into the domain is modeled by a source centered at the left boundary. The flow is described using Cartesian coordinates $(x, y) \in [0, L_x] \times [0, L_y]$. The $\boldsymbol{E} \times \boldsymbol{B}$ drift velocity is given by $\boldsymbol{v}_E = (\boldsymbol{E} \times \boldsymbol{B})/B_0^2$, where $B_0 = ||\boldsymbol{B}||$. We make the electrostatic approximation such that $\boldsymbol{E} = -\nabla\phi$ and define the normalized velocity field $\boldsymbol{v} = (v_x, v_y)^\top$ as

$$\boldsymbol{v} = B_0 \boldsymbol{v}_{E\perp} = (\boldsymbol{e}_z \times \nabla\phi)_\perp = \begin{pmatrix} -\partial_y \phi \\ \partial_x \phi \end{pmatrix}. \tag{4a}$$

Let Ω denote the z-component of the normalized vorticity vector $\boldsymbol{\Omega} = \nabla \times B_0 \boldsymbol{v}_E = (\partial_x v_y - \partial_y v_x)\boldsymbol{e}_z$. Then, the normalized electrostatic potential is obtained from

$$\nabla_\perp^2 \phi = \Omega. \tag{4b}$$

To describe the evolution of the pressure $p(x, y, t)$ and the vorticity $\Omega(x, y, t)$, we employ a normalized convection model

$$\left(\frac{\partial}{\partial t} + \boldsymbol{v} \cdot \nabla_\perp\right) p = \kappa \nabla_\perp^2 p + S(x), \tag{4c}$$

$$\left(\frac{\partial}{\partial t} + \boldsymbol{v} \cdot \nabla_\perp\right) \Omega + \frac{\partial p}{\partial y} = \nu \nabla_\perp^2 \Omega. \tag{4d}$$

Here, κ is the diffusion coefficient, ν is the viscosity, and $S(x)$ is a pressure source. We choose the source as a Gaussian function of x centered at the left boundary

$$S(x) = q e^{-\frac{x^2}{2\sigma^2}}. \tag{4e}$$

The parameter q determines the strength of the source and σ determines the width of the source. At the $y = 0$ and $y = L_y$ boundaries, we apply periodic boundary conditions. For the pressure, we apply a Neumann boundary condition at the left boundary, $\partial_x p(0, y, t) = 0$, and a Dirichlet boundary condition at the right boundary, $p(L_x, y, t) = 0$. These boundary conditions allow the pressure gradient to increase as the source strength, q, increases. For the electrostatic potential and vorticity, we apply Dirichlet boundary conditions at both the left and right boundaries, $\Omega(0, y, t) = \Omega(L_x, y, t) = 0$, $\phi(0, y, t) = \phi(L_x, y, t) = 0$. As initial condition, each of the system variables is set to zero at $t = 0$. System (4) is one of the simplest models used to describe nonlinear plasma dynamics. Bian *et al.*[19] and Garcia *et al.*[20] model the resistive g-instability in a plasma fluid layer with a system similar to (4). Refs. 21–23 model the interchange motions of isolated structures in magnetized plasmas with a system equivalent to (4). In the field of fluid dynamics, the system is often used to model Rayleigh-Bénard convection.[24] More accurate models for nonlinear plasma dynamics like the ESEL model[25,26] can be regarded as extensions to the convection model (4) by including additional terms and couple more fields to describe more nonlinear effects.

A. State variable definitions

Predator-prey models for the L–H transition are often based on three state variables; the potential energy related to the pressure profile, the turbulent flow, and the zonal flow. To formally define these variables in terms of the state variables of the PDE system (4), we first introduce some useful notation: An overline denotes average over the y-variable, a tilde denotes the spatial fluctuations, and angle brackets denote average over the x-variable

$$\bar{f}(x, t) = \frac{1}{L_y} \int_0^{L_y} f(x, y, t)\, dy,$$

$$\tilde{f}(x, y, t) = f(x, y, t) - \bar{f}(x, t),$$

$$\langle \bar{f} \rangle(t) = \frac{1}{L_x} \int_0^{L_x} \bar{f}(x, t)\, dx.$$

To consistently define the state variables, we consider (4) with unchanged boundary conditions in the limit of no source, no viscosity, and no diffusivity. Averaging (4c) with $\kappa = S = 0$ over y and x, followed by integration by parts, gives

$$\partial_t \langle \bar{p} \rangle = -\langle \overline{v_x (\partial_x p)} \rangle - \langle \overline{v_y (\partial_y p)} \rangle = \langle \overline{(\partial_x v_x + \partial_y v_y) p} \rangle = 0.$$

Since the average of p is constant in time, even when the pressure drives a flow, it cannot be used as a measure for the potential energy of the system. If we instead consider (4c) with $\kappa = S = 0$, multiply by x, and then average over y and x, we obtain

$$\partial_t \langle \overline{xp} \rangle = \langle \overline{v_x p} \rangle. \tag{5}$$

The spatially averaged kinetic energy of the flow is given by $K = \frac{1}{2} \langle \overline{\boldsymbol{v} \cdot \boldsymbol{v}} \rangle$. Considering (4d) with $\nu = 0$, multiplying by ϕ, and using integration by parts, it can be shown that

$$\frac{1}{2} \partial_t \langle \overline{\boldsymbol{v} \cdot \boldsymbol{v}} \rangle = -\langle \overline{\phi (\partial_t \Omega)} \rangle = -\langle \overline{v_x p} \rangle. \tag{6}$$

Adding (5) and (6) gives the conservation equation

$$\partial_t \left(\frac{1}{2} \langle \overline{\boldsymbol{v} \cdot \boldsymbol{v}} \rangle + \langle \overline{xp} \rangle \right) = 0. \tag{7}$$

Since the first term in (7) is the time derivative of the kinetic energy, we define the second term to be the time derivative of the potential energy. We now separate the kinetic energy into the zonal flow energy and the fluctuation energy. Inserting the decomposition $v_x = \bar{v}_x + \tilde{v}_x$ with $\bar{v}_x = 0$ and $v_y = \bar{v}_y + \tilde{v}_y$ into the expression $\boldsymbol{v} \cdot \boldsymbol{v}$ and averaging over y and x gives

$$\frac{1}{2} \langle \overline{\boldsymbol{v} \cdot \boldsymbol{v}} \rangle = \frac{1}{2} \langle \overline{\tilde{v}_x^2} + \overline{\tilde{v}_y^2} \rangle + \frac{1}{2} \langle \bar{v}_y^2 \rangle. \tag{8}$$

The first term on the right-hand side is the kinetic energy related to the fluctuations, while the second term is the kinetic energy related to the zonal flow.

We can now define the average potential energy, P, related to the pressure profile, the average fluctuation energy, N, and the zonal flow energy, F, by

$$P = \langle \overline{xp} \rangle, \quad N = \frac{1}{2} \langle \overline{\tilde{v}_x^2} + \overline{\tilde{v}_y^2} \rangle, \quad F = \frac{1}{2} \langle \bar{v}_y^2 \rangle. \tag{9}$$

Sugama and Horton,[4] and Dewar, and Sugama[5] define state variables for their L–H transition models which are equivalent to the definitions in (9).

The time-derivatives of the energies (9) for the system (4a) can be written as

$$\dot{P} = q\frac{\sigma^2}{L_x}\left(1 - \mathrm{e}^{-\frac{L_x^2}{2\sigma^2}}\right) + \kappa\langle\overline{x\partial_{xx}^2 p}\rangle + \langle\overline{v_x p}\rangle, \tag{10a}$$

$$\dot{N} = -\langle\overline{v_x p}\rangle - \nu\langle\overline{\Omega^2}\rangle - \nu\langle\bar{v}_y\partial_{xx}^2\bar{v}_y\rangle + \langle\bar{v}_y\partial_x\overline{\tilde{v}_x\tilde{v}_y}\rangle, \tag{10b}$$

$$\dot{F} = -\langle\bar{v}_y\partial_x\overline{\tilde{v}_x\tilde{v}_y}\rangle + \nu\langle\bar{v}_y\partial_{xx}^2\bar{v}_y\rangle. \tag{10c}$$

A physical modeling approach would use this set of equations as a starting point. In (10a), the source term, which is proportional to q, causes an increase in P. The diffusion term dampens P. The last term in (10a) and the first term in (10b) are the pressure energy flux that transfers energy between the potential energy and the turbulent flow energy. The first viscosity term in (10b), $\nu\langle\overline{\Omega^2}\rangle$, suppresses N, while the two last terms are equal to $-\dot{F}$. The last term in (10b) and the first term in (10c) derive from the Reynolds stress, $\overline{\tilde{v}_x\tilde{v}_y}$. The Reynolds stress is generated by the turbulent flow and drives the zonal flow. The last term in (10c) dampens the zonal flow energy due to viscosity.

B. Parameters and numerical solver

We fix all parameter values except q which we consider as a bifurcation parameter. The values of the fixed parameters in (4) are listed in Table I. The bifurcation parameter q is fixed for each simulation, but we consider multiple simulation data sets obtained for different values of $q \in [0, 10]$. The FEM software package COMSOL Multiphysics® is used as the numerical solver.[27] The PDE system (4) and the corresponding boundary conditions are defined on the rectangular domain $[0, L_x] \times [0, L_y]$. To obtain the required simulation data, we use a triangular mesh containing 6282 domain elements. The solution is initialized at $t = 0$ and run with output time steps of $\Delta t = 0.05$ until $t = 400$. At each output time of the simulation, the three energies (9) and their time-derivatives are computed and saved.

C. Solution parameter dependency

Simulation data were obtained for multiple values of $q \in [0, 10]$. As q varies, we observe four qualitatively different types of solutions. In the (P, N, F)-state space, each solution type is characterized by the stability type of the observed equilibrium points.

For $q = 2$, the solution to (4) converges to a static solution. Here, the pressure is independent of the y-coordinate, and there is no vorticity and therefore no flow. For the time evolution of the energies, P converges to a positive constant value, while $N = F = 0$ for all time. We denote the equilibrium (P_s, N_s, F_s) corresponding to this static state the s-equilibrium.

For $q = 6$, the solution converges to a stable solution, where p and v_x are symmetric, while Ω and v_y are antisymmetric through a line at $y = 1/2$. The time evolution of the energies P, N, and F contains two phases: The first phase is similar to the solution for $q = 2$, where $N = F = 0$ while P approaches an equilibrium value. However, this equilibrium solution is unstable and, during the second phase, N first increases rapidly and then decreases toward an equilibrium value. This causes P to make a little bump on the curve and then decreases toward a lower stable equilibrium value. Since v_x and v_y are nonzero almost everywhere there is a non-zonal flow, $N > 0$, while the symmetry of v_x and the antisymmetry of v_y cause the vanishing zonal flow, $F = 0$. The potential energy of the pressure, P, is a measure of the level of plasma confinement. Since this state results in the lowest confinement level of the four states, we denote this state the low confinement state and the corresponding equilibrium point (P_L, N_L, F_L) is denoted as the L-equilibrium.

For $q = 8$, the solution converges to the down-drifting patterns shown in Fig. 1. The symmetry of the patterns that exist for $q = 6$ is now broken. The time evolution of the energies P, N, and F is shown in Fig. 2. The solution now consists of three phases: The first two phases are similar to the solution phases for $q = 6$. In the third phase, F increases and approaches an equilibrium value. This causes P to converge to a larger equilibrium value and N to converge to a smaller equilibrium value. Compared to the $q = 6$ solution, breaking of the symmetry of v_x and v_y causes the zonal flow, $F > 0$. Since this state results in a higher confinement than before we denote this state the high confinement state, the corresponding equilibrium point (P_H, N_H, F_H) is denoted as the H-equilibrium.

For $q = 10$, the solution converges to oscillating patterns. p is oscillating between two clearly different patterns, while the patterns for Ω, v_x, and v_y are mostly oscillating in terms of amplitude. The time evolution of the energies still consists of three phases similarly to the solution for $q = 8$. However, the third phase is now replaced by convergence to

TABLE I. The fixed parameter values for the system (4). $q \in [0, 10]$ is a bifurcation parameter.

L_x	L_y	κ	ν	σ
1.0	1.0	0.05	0.05	0.1

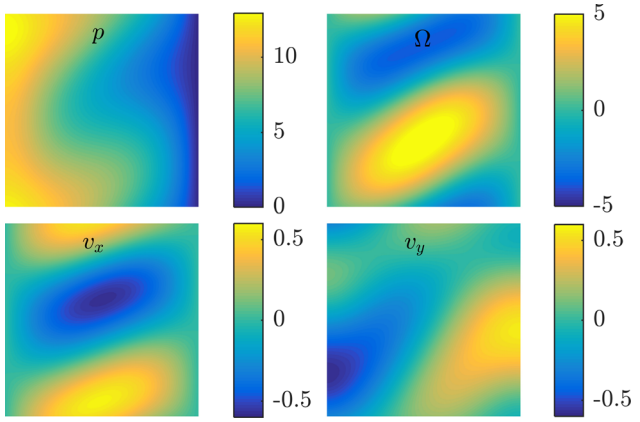

FIG. 1. The $q = 8$ high confinement solution at $t = 200$ showing p (upper left), Ω (upper right), v_x (lower left), and v_y (lower right). The patterns are in motion and are drifting downward for increasing time.

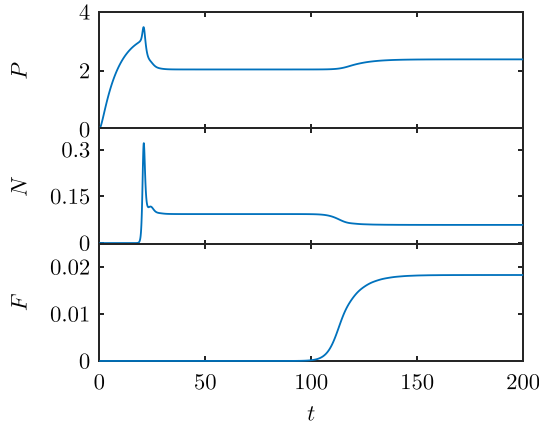

FIG. 2. The $q = 8$ time evolution of the energies P, N, and F. The solution converges to the H-equilibrium, where all three energies are positive.

a stable limit cycle, where the three energies oscillate at identical frequencies. We denote this solution type as the limit cycle solution.

D. Data-based bifurcation diagram

Simulation data for P, N, and F were generated for $q \in \{0, 0.1, \ldots, 10\}$. For $q > 10$, more bifurcations occur, with the first one being a period doubling bifurcation. Hence, the dynamics is getting increasingly more complex and it is unlikely that can be described by one simple ODE model. Hence, we limit the identification to be based on this range of q-values. The data-based bifurcation diagram shown in Fig. 3 is constructed by approximately identifying the location of all equilibrium points for each solution. The unstable

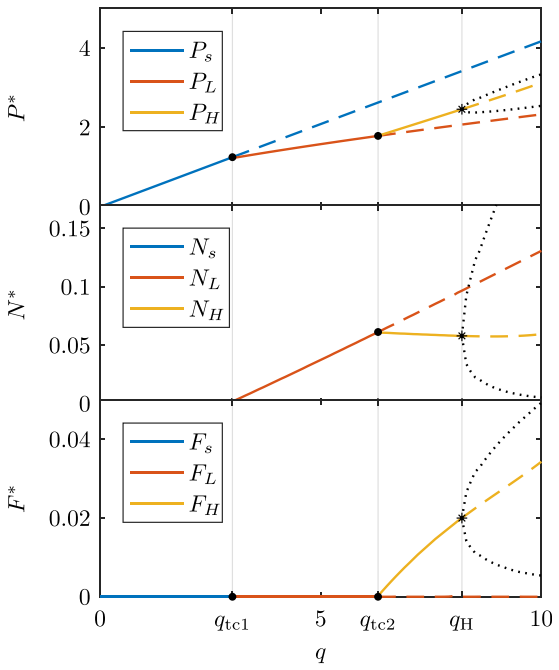

FIG. 3. Bifurcation diagram generated from simulation data. Solid curves are stable equilibrium points, dashed curves are unstable equilibrium points, while the dotted curves show the amplitude of the stable limit cycle. The transcritical bifurcations occurring at approximately $q_{tc1} \approx 2.92$ and $q_{tc2} \approx 6.28$ are marked with dots, while the Hopf bifurcation occurring at $q_H \approx 8.15$ is marked with asterisks.

s-equilibrium is computed from a modified model with $v = 0$, the unstable L-equilibrium is estimated from the transient part of the solution, and the unstable H-equilibrium is extrapolated from the stable part of the H-equilibrium. Transcritical bifurcations occur at approximately $q_{tc1} \approx 2.92$ and $q_{tc2} \approx 6.28$, while a Hopf bifurcation occurs at $q_H \approx 8.15$. The s-equilibrium is stable for $0 \le q < q_{tc1}$, the L-equilibrium is stable for $q_{tc1} < q < q_{tc2}$, the H-equilibrium is stable for $q_{tc2} < q < q_H$, and the limit cycle is stable for $q > q_H$. When a model for the dynamics of the energies P, N, and F has been identified, we compare a bifurcation diagram for the model with this data-based bifurcation diagram. The level of similarity between the diagrams will be used as one of the measures of how well the model fits the data.

IV. IDENTIFICATION OF TRANSITION DYNAMICS WITH SINDy

As shown in Fig. 3, the simulation data transition between four qualitatively different types of solutions when q varies in $[0, 10]$. We identify the governing system by modeling the four states of the system stepwise to progressively include more complicated dynamics in the model. We restrict the candidate polynomials of the model to be up to second order. It is observed that the inclusion of third order polynomials fails to improve the model further. The quality of the model is determined by visually comparing how well the model describes the position of equilibrium points and how well solutions to the model reproduce the simulated time series data.

A. Modeling the s-state

When $q < q_{tc1}$, the solution converges to the static equilibrium, where $P > 0, N = F = 0$. We apply the SINDy algorithm to identify the governing equation for the time evolution of P. For this, we use simulation data generated by solving (4) for $q \in \{0.0, 0.1, \ldots, 2.9\}$ such that the data include 30 time series of $P(t)$ and $\dot{P}(t)$ at increasing q-values. We choose as candidate functions a linear function of q, and first and second order polynomial terms of P

$$\Theta(\boldsymbol{q}, \boldsymbol{P}) = \begin{bmatrix} \boldsymbol{q} & \boldsymbol{P} & \boldsymbol{P}^2 \end{bmatrix}.$$

From the simulation data, SINDy identifies the following sparse model:

$$\dot{P} = rq - \chi P \tag{11}$$

with $r = 4.311 \times 10^{-2}$ and $\chi = 0.1031$. Comparing (11) with (4c), we see that the first term on the right-hand side of (11) derives from the source term S and the second term derives from the diffusion term, $\kappa \nabla_\perp^2 p$. The model (11) has the unique equilibrium point $P_s = rq/\chi$. The plot in Fig. 4 compares the values of P_s as a function of q for the simulation data and the model. The position of the s-equilibrium is accurately described by the model. Figure 5 shows comparisons of the time series data for P and solutions to the model (11) with initial condition $P(0) = 0$ for three different values of q. The model solutions approximate the dynamics of the

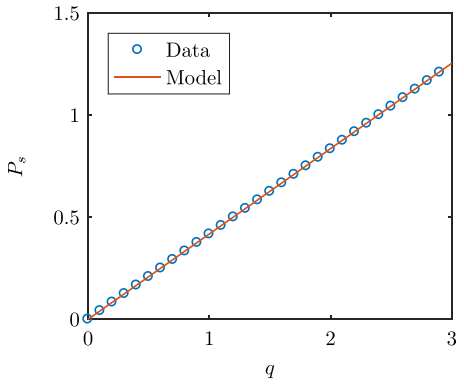

FIG. 4. The static equilibrium value P_s as a function of q for the data (circles) and the model (solid line).

simulation data sufficiently well that we will be using this model to describe the s-state.

B. Modeling the L-state

When $q_{\mathrm{tc1}} < q < q_{\mathrm{tc2}}$, the solution converges to the L-equilibrium, where $P, N > 0$ and $F = 0$. We apply the SINDy method to identify the underlying system for the time evolution of P and N. For this, we use simulation data for $q = \{0.0, 0.1, \ldots, 6.2\}$. We restrict the equations for $\dot{P}$ and $\dot{N}$ to be up to second order polynomials

$$\Theta(\boldsymbol{q}, \boldsymbol{P}, \boldsymbol{N}) = \begin{bmatrix} \boldsymbol{q} & \boldsymbol{P} & \boldsymbol{N} & \boldsymbol{P^2} & \boldsymbol{PN} & \boldsymbol{N^2} \end{bmatrix}.$$

To pass on the parameter values previously determined, we model $\dot{P} - rq + \chi P$ with the values of r and χ determined in Section IV A. With these settings, the SINDy algorithm identifies the following model:

$$\dot{P} = rq - \chi P - \eta_1 N - \eta_2 N^2 + \eta_3 NP, \tag{12a}$$

$$\dot{N} = N(\gamma P - \beta_1 - \beta_2 N) \tag{12b}$$

with $r = 4.311 \times 10^{-2}$, $\chi = 0.1031$, $\eta_1 = 7.317$, $\eta_2 = 41.13$, $\eta_3 = 4.700$, $\gamma = 1.953$, $\beta_1 = 2.422$, $\beta_2 = 17.72$. The model (12) for the L-state reduces to the model (11) for the s-state when $N = 0$ as intended. In (12a), three additional terms have been added when compared with (11). When the L-equilibrium becomes stable and N converges to the positive value N_L then P converges to P_L which is smaller than P_s. So the fluctuating energy N causes a decrease in P. This effect is modeled by the two terms with coefficients η_1 and η_2. When N initially begins to increase, the value of P also increases temporarily, resulting in a little bump on the curve of $P(t)$. This effect is described by the term with coefficient η_3. Equation (12b) describes the evolution of the fluctuation energy N. When the pressure gradient becomes sufficiently steep, the constant profile characterizing the s-solution becomes unstable and a fluctuating flow is generated. This effect is modeled in (12b) by the term with coefficient γ. Dissipation causes the fluctuation energy N to be self-damped. This is described by the terms with coefficients β_1 and β_2. The L-equilibrium becomes stable at a transcritical bifurcation at $q_{\mathrm{tc1}} = \beta_1 \chi/(\gamma r) = 2.967$ which is close to the data-derived value of $q_{\mathrm{tc1}} \approx 2.92$. The plots in Fig. 6 compare P_L and N_L as functions of q for the simulation data and the model. The model approximates the position of the L-equilibrium well. Figure 7 shows comparisons of the simulation data and solutions to the model (12) for three different values of q. As initial conditions for (12), we used $P(0) = 0$, while $N(0)$ was chosen to make the initial increase in N fit the corresponding simulation data: $N(0) = 1 \times 10^{-9}$ for $q = 4$, $N(0) = 2 \times 10^{-11}$ for $q = 5$, and $N(0) = 2.5 \times 10^{-12}$ for $q = 6$. The plots in Fig. 7 show that the small bump in the curve of $P(t)$ created by the sudden increase in $N(t)$ is captured by the model. The fast increase in N and the subsequent monotonic decrease to the equilibrium value N_L are also contained in the model. Since the model captures the position of the L-equilibrium and approximately reproduces the time series data quantitatively correct, we will use this model to describe the L-state.

C. Modeling the H-state and the limit cycle state

When $q_{\mathrm{tc2}} < q < q_{\mathrm{H}}$, the solution converges to the H-equilibrium, where $P, N, F > 0$. For $q > q_{\mathrm{H}}$, the H-equilibrium is unstable and the solution converges to a limit cycle. We apply SINDy to identify the governing equations for both of these states simultaneously. The system is identified in the space of polynomials (P, N, and F) up to the second order

$$\Theta(\boldsymbol{q}, \boldsymbol{P}, \boldsymbol{N}, \boldsymbol{F}) = \begin{bmatrix} \boldsymbol{q} & \boldsymbol{P} & \boldsymbol{N} & \boldsymbol{F} & \boldsymbol{P^2} & \boldsymbol{PN} & \cdots & \boldsymbol{F^2} \end{bmatrix}.$$

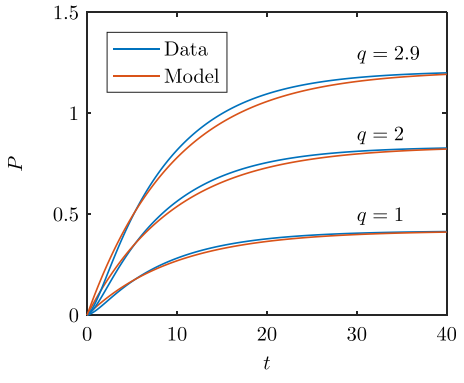

FIG. 5. The time evolution of P as given by the simulation data and by the model for different values of q.

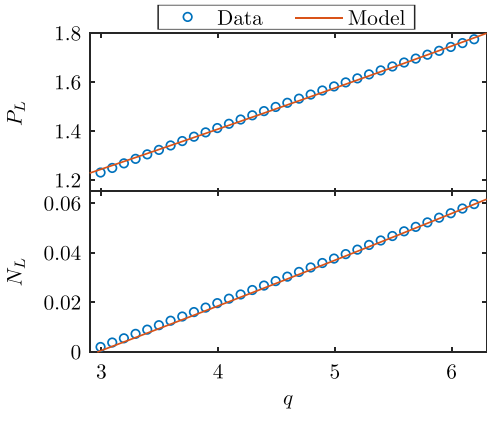

FIG. 6. P_L (top) and N_L (bottom) as functions of q for the data (circles) and the model (solid lines).

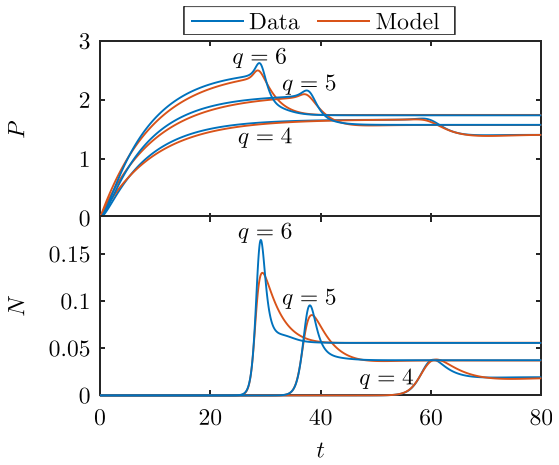

FIG. 7. Comparisons of the time evolution of P (top) and N (bottom) as given by the simulation data and for the model solution for different values of q.

We again restrict the model to contain the previously found terms, i.e., instead of identifying equations for $\dot{P}$ and $\dot{N}$ directly we identify equations for $\dot{P} - rq + \chi P + \eta_1 N + \eta_2 N^2 - \eta_3 NP$ and $\dot{N} - N(\gamma P - \beta_1 - \beta_2 N)$ with the previously determined coefficients. In this case, SINDy identifies different models depending on which values of q we include data for. This indicates that the dynamics cannot be accurately described in terms of the candidate polynomials. In the data-based bifurcation diagram in Fig. 3, we see that when the H-equilibrium is stable, P_H and F_H are increasing as functions of q, while N_H is slightly decreasing as a function of q. When including data for $q \in \{0.0, 0.1, \ldots, 9.2\}$, SINDy identifies the equation for the time evolution of F as $\dot{F} = F(\alpha_2 N - \mu)$. This expression makes $N_H = \mu/\alpha_2$ independent of q. When including data for $q \in \{0.0, 0.1, \ldots, 10.0\}$, SINDy identifies the equation for the time evolution of F as $\dot{F} = F(\alpha_2 N - \mu P)$. This gives a linear relationship between N_H and P_H, and both P_H and N_H are increasing as functions of q. None of these expressions describe the N_H-dependency of q qualitatively correct. However, the first expression for $\dot{F}$ approximates the behavior better than the second expression, so we retain that. For the equations for $\dot{P}$ and $\dot{N}$, we use the result obtained when including data for $q \in \{0.0, 0.1, \ldots, 10.0\}$. This results in the model

$$\dot{P} = rq - \chi P - \eta_1 N - \eta_2 N^2 + \eta_3 PN - \varphi_1 F - \varphi_2 F^2 + \varphi_3 PF, \tag{13a}$$

$$\dot{N} = N(\gamma P - \beta_1 - \beta_2 N - \alpha_1 F), \tag{13b}$$

$$\dot{F} = F(\alpha_2 N - \mu). \tag{13c}$$

The coefficients identified by SINDy result in a poor approximation of the position of the H-equilibrium as a function of q. Instead, the ratio μ/α_2 is chosen to reproduce the data-derived value of q_{tc2} in the model. The value of α_1 is determined by a linear fit to a plot of $\gamma P_H - \beta_1 - \beta_2 N_H$ as a function of F_H. The value of α_2 is chosen to approximately reproduce the frequency of the oscillations. Finally, φ_1, φ_2, and φ_3 are computed to obtain the best possible approximation of F_H as a function of q and to reproduce the data-derived value of q_H in the model. Table II lists the parameter values for (13).

TABLE II. The parameter values for the system (13). $q \in [0, 10]$ is a bifurcation parameter.

r	χ	η_1	η_2	η_3	γ	β_1
4.311×10^{-2}	0.1031	7.317	41.13	4.700	1.953	2.422
β_2	φ_1	φ_2	φ_3	α_1	α_2	μ
17.72	70.50	1151	34.12	63.32	33.00	2.023

In (13a), the zonal flow energy enters into the equation for $\dot{P}$ similarly to the turbulent flow. In (13b), the zonal flow suppresses the turbulent flow and in (13c), the turbulent flow drives the zonal flow. This predator-prey type coupling between the zonal flow and the turbulent flow is attributable to the Reynolds stress. The zonal flow energy is linearly self-damping due to the viscosity term. Near the H-equilibrium the zonal flow dampens P, but the zonal flow also dampens N, which causes a decrease in the damping of P, so the overall effect is that P increases when F increases.

The plots in Fig. 8 compare P_H, N_H, and F_H as functions of q for the simulation data and the model. The model approximates the value of F_H accurately, since the parameter values were chosen to obtain the best possible fit of F_H as a function of q for the model. The model also approximates P_H and N_H within a small relative error. The plots in Figs. 9 and 10 compare the simulation data and the model solutions for $q = 7$ and $q = 10$, respectively. The initial conditions were chosen such that N and F begin to increase at about the same time as in the corresponding data. For $q = 7$, the initial condition for the model solution shown in Fig. 9 was $(P(0), N(0), F(0)) = (0, 1 \times 10^{-12}, 1 \times 10^{-28})$. For the model solution, F increases a little faster than the corresponding data, but otherwise the model solution approximates the data very well both qualitatively and quantitatively. For $q = 8$, the model solution (not shown) spirals into the H-equilibrium, while the corresponding data approach the H-equilibrium monotonically.

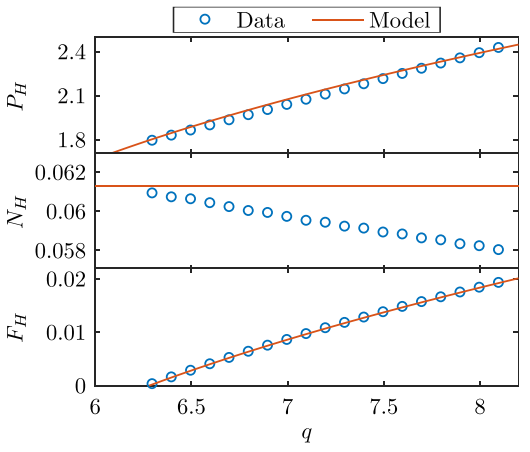

FIG. 8. P_H (top), N_H (middle), and F_H (bottom) as functions of q for the data (circles) and the model (solid lines).

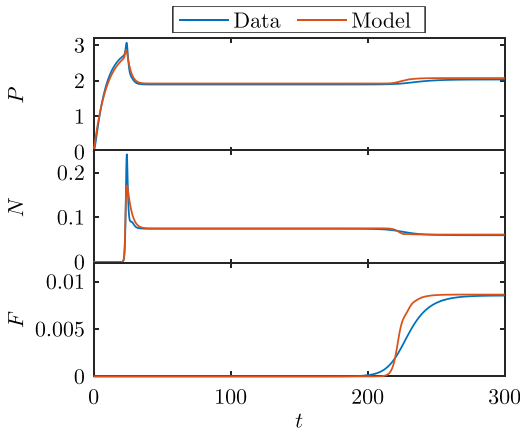

FIG. 9. Comparison of the time evolution of P (top), N (middle), and F (bottom) for the simulation data and for the model solution for $q = 7$.

Otherwise the model solution approximates the data very well. For $q = 9$, the model solution (not shown) converges to a stable limit cycle like the data. The model fails to reproduce the amplitude and frequency of the oscillations. For $q = 10$, the initial condition for the model solution shown in Fig. 10 was $(P(0), N(0), F(0)) = (0, 1 \times 10^{-13}, 1 \times 10^{-53})$. The model solution still converges to a stable limit cycle like the data. The model solution now correctly reproduces the frequency of the oscillations, but it fails to reproduce the amplitude of the oscillations. The mean value of P during the oscillations is lower for the model solution than for the data. This might indicate that we are approaching the maximum value of q for which the model is valid. The failure to reproduce the correct amplitude of the oscillations is expected, since amplitude fitting was not chosen as a criterion during the modeling process. Overall, the final model (13) reproduces the simulation data very well both qualitatively and quantitatively for $q \in [0, 10]$.

V. BIFURCATION ANALYSIS

Using the SINDy algorithm, we have derived the model (13) with the parameters listed in Table II for the time evolution of the three energies P, N, and F computed from solutions to the convection problem (4). We now carry out a bifurcation analysis for the model (13) and summarize the results in a bifurcation diagram.

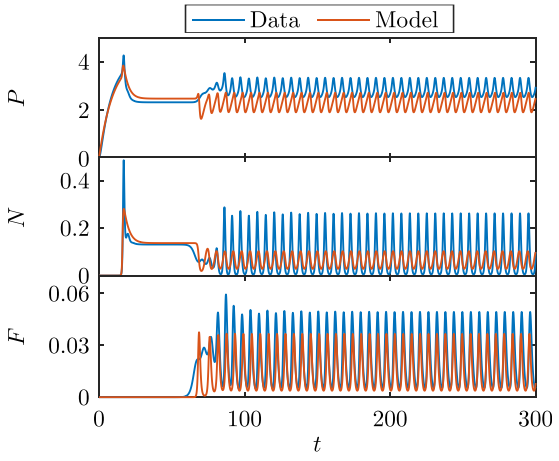

FIG. 10. Comparison of the time evolution of P (top), N (middle), and F (bottom) for the simulation data and for the model solution for $q = 10$.

A. Equilibrium points

The system has a total of five equilibrium points, but we only list and name the three equilibrium points which are stable for some value of $q \in [0, 10]$. The s-equilibrium is

$$(P_s, N_s, F_s) = \left(\frac{r}{\chi} q, 0, 0\right), \quad q > 0. \tag{14}$$

The L-equilibrium enters the physical domain in a transcritical bifurcation at $q = q_{tc1} = \beta_1 \chi/(\gamma r)$. Define

$$\begin{aligned} a_{P_L} &= \gamma(\beta_2 \eta_3 - \gamma \eta_2), \\ b_{P_L} &= -(\beta_1 \beta_2 \eta_3 + \beta_2^2 \chi + \beta_2 \gamma \eta_1 - 2\beta_1 \gamma \eta_2), \\ c_{P_L} &= \beta_2^2 r q + \beta_1 \beta_2 \eta_1 - \beta_1^2 \eta_2 \end{aligned}$$

and

$$\begin{aligned} a_{N_L} &= \beta_2 \eta_3 - \gamma \eta_2, \\ b_{N_L} &= -(\beta_2 \chi + \gamma \eta_1 - \beta_1 \eta_3), \\ c_{N_L} &= \gamma r q - \beta_1 \chi. \end{aligned}$$

Then, the components of the L-equilibrium (P_L, N_L, F_L), $q > q_{tc1}$ are

$$P_L = \frac{1}{2a_{P_L}} \left(-b_{P_L} - \sqrt{b_{P_L}^2 - 4a_{P_L} c_{P_L}}\right), \tag{15a}$$

$$N_L = \frac{1}{2a_{N_L}} \left(-b_{N_L} - \sqrt{b_{N_L}^2 - 4a_{N_L} c_{N_L}}\right), \tag{15b}$$

$$F_L = 0. \tag{15c}$$

The H-equilibrium enters the physical domain in a transcritical bifurcation at $q = q_{tc2}$, where

$$q_{tc2} = \frac{1}{\gamma r} \left(\beta_1 \chi - b_{N_L} \frac{\mu}{\alpha_2} - a_{N_L} \frac{\mu^2}{\alpha_2^2}\right).$$

We define

$$\begin{aligned} a_{P_H} &= \alpha_2^2 \gamma(\gamma \varphi_2 - \alpha_1 \varphi_3), \\ b_{P_H} &= -\alpha_2(\alpha_1^2 \eta_3 \mu - \alpha_1^2 \alpha_2 \chi - \alpha_1 \alpha_2 \beta_1 \varphi_3 - \alpha_1 \alpha_2 \gamma \varphi_1 \\ &\quad -\alpha_1 \beta_2 \mu \varphi_3 + 2\alpha_2 \beta_1 \gamma \varphi_2 + 2\beta_2 \gamma \mu \varphi_2), \\ c_{P_H} &= -(\alpha_1^2 \alpha_2^2 r q - \alpha_1^2 \alpha_2 \eta_1 \mu - \alpha_1^2 \eta_2 \mu^2 + \alpha_1 \alpha_2^2 \beta_1 \varphi_1 \\ &\quad +\alpha_1 \alpha_2 \beta_2 \mu \varphi_1 - \alpha_2^2 \beta_1^2 \varphi_2 - 2\alpha_2 \beta_1 \beta_2 \mu \varphi_2 - \beta_2^2 \mu^2 \varphi_2) \end{aligned}$$

and

$$\begin{aligned} a_{F_H} &= \alpha_2^2(\gamma \varphi_2 - \alpha_1 \varphi_3), \\ b_{F_H} &= \alpha_2(\alpha_1 \alpha_2 \chi - \alpha_1 \eta_3 \mu - \alpha_2 \beta_1 \varphi_3 + \alpha_2 \gamma \varphi_1 - \beta_2 \mu \varphi_3), \\ c_{F_H} &= -(\alpha_2^2 \gamma r q - \alpha_2^2 \beta_1 \chi + \alpha_2 \beta_1 \eta_3 \mu - \alpha_2 \beta_2 \chi \mu \\ &\quad -\alpha_2 \eta_1 \gamma \mu + \beta_2 \eta_3 \mu^2 - \eta_2 \gamma \mu^2). \end{aligned}$$

Then, the H-equilibrium can be written as (P_H, N_H, F_H), $q > q_{tc2}$ with

$$P_H = \frac{1}{2a_{P_H}}\left(-b_{P_H} + \sqrt{b_{P_H}^2 - 4a_{P_H}c_{P_H}}\right), \tag{16a}$$

$$N_H = \frac{\mu}{\alpha_2}, \tag{16b}$$

$$F_H = \frac{1}{2a_{F_H}}\left(-b_{F_H} + \sqrt{b_{F_H}^2 - 4a_{F_H}c_{F_H}}\right). \tag{16c}$$

B. Stability of equilibrium points

The stability type of the equilibrium points is determined by the eigenvalues of the Jacobian matrix of (13) evaluated at the equilibrium point. Let $\boldsymbol{A}_s$ denote the Jacobian matrix evaluated at the static equilibrium. $\boldsymbol{A}_s$ is an upper triangular matrix, so the eigenvalues are given by the diagonal elements

$$\lambda_1 = -\chi, \quad \lambda_2 = \frac{\gamma r}{\chi}q - \beta_1, \quad \lambda_3 = -\mu.$$

All three eigenvalues are real. λ_1 and λ_3 are negative constants, while λ_2 is negative for $q < q_{tc1}$ and positive for $q > q_{tc1}$. So the s-equilibrium is a stable node for $q < q_{tc1}$ and a saddle for $q > q_{tc1}$.

Denote the Jacobian matrix evaluated at the L-equilibrium by $\boldsymbol{A}_L$. Define

$$b_L = \beta_2 N_L + \chi - \eta_3 N_L,$$
$$c_L = -N_L((\beta_2\eta_3 - 2\gamma\eta_2)N_L + \gamma\eta_3 P_L - \beta_2\chi - \gamma\eta_1).$$

Then, the eigenvalues of $\boldsymbol{A}_L$ are

$$\lambda_1 = -\frac{1}{2}\left(b_L - \sqrt{b_L^2 - 4c_L}\right),$$
$$\lambda_2 = -\frac{1}{2}\left(b_L + \sqrt{b_L^2 - 4c_L}\right),$$
$$\lambda_3 = \alpha_2 N_L - \mu.$$

$\mathrm{Re}(\lambda_1)$ is positive for $q < q_{tc1}$ and negative for $q > q_{tc1}$, while $\mathrm{Re}(\lambda_2) < 0$ for all q. $\mathrm{Re}(\lambda_3)$ is negative for $q < q_{tc2}$ and positive for $q > q_{tc2}$. So the L-equilibrium is a saddle for $q < q_{tc1}$. It is a stable node or stable focus-node for $q_{tc1} < q < q_{tc2}$ and a saddle-focus or an unstable node for $q > q_{tc2}$.

Denote the Jacobian matrix evaluated at the H-equilibrium by $\boldsymbol{A}_H$. Let $\tau = \mathrm{Tr}(\boldsymbol{A}_H)$ be the trace, σ the sum of principal minors, and $\delta = \det(\boldsymbol{A}_H)$ the determinant of $\boldsymbol{A}_H$

$$\tau = -\chi + \eta_3 N_H + \varphi_3 F_H - \beta_2 N_H,$$
$$\sigma = N_H(\alpha_1\alpha_2 F_H + \beta_2\chi - \beta_2\eta_3 N_H - \beta_2\varphi_3 F_H,$$
$$\quad +\gamma\eta_1 + 2\gamma\eta_2 N_H - \gamma\eta_3 P_H)$$
$$\delta = \alpha_2 N_H F_H(-\alpha_1\chi + \alpha_1\eta_3 N_H + \alpha_1\varphi_3 F_H$$
$$\quad -\gamma\varphi_1 - 2\gamma\varphi_2 F_H + \gamma\varphi_3 P_H).$$

Then, the characteristic polynomial is given by

$$p(\lambda) = \lambda^3 - \tau\lambda^2 + \sigma\lambda - \delta.$$

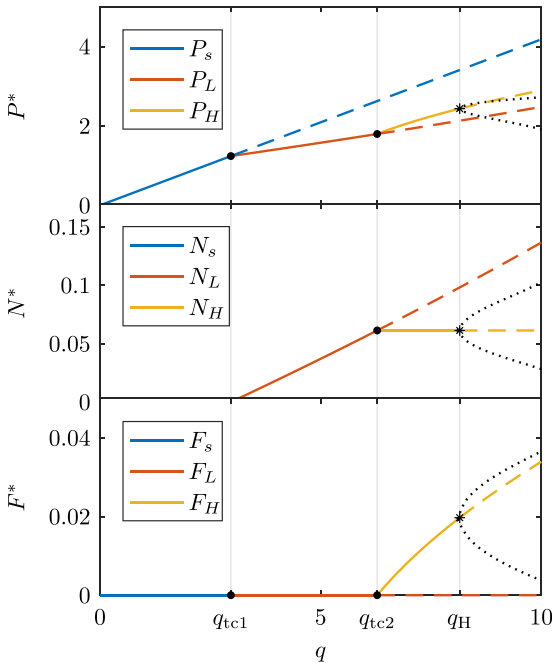

FIG. 11. Bifurcation diagram for the model. Solid curves are stable equilibrium points, dashed curves are unstable equilibrium points, while the dotted curve shows the amplitude of the limit cycle solution. The transcritical bifurcations occurring at approximately $q_{tc1} = 2.967$ and $q_{tc2} = 6.281$ are marked with dots, while the Hopf bifurcation occurring at $q_H = 8.152$ is marked with asterisks.

The eigenvalues are obtained as the three complex solutions to $p(\lambda) = 0$. Inserting $\lambda = i\omega$ and solving $p(i\omega) = 0$ show that a Hopf bifurcation occurs when $\sigma\tau = \delta$. By numerically solving this equation for q, we obtain $q_H = 8.152$. The eigenvalue λ_1 is positive for $q < q_{tc2}$ and negative for $q > q_{tc2}$. $\mathrm{Re}(\lambda_2)$ and $\mathrm{Re}(\lambda_3)$ are negative for $q < q_H$ and positive for $q > q_H$. So the H-equilibrium is a saddle or a saddle-focus for $q < q_{tc2}$, it is a stable focus-node for $q_{tc2} < q < q_H$, and it is a saddle-focus for $q > q_H$.

C. Bifurcation diagram

The positions and the stability of the equilibrium points for (13) as functions of q are summarized in the bifurcation diagram in Fig. 11. A comparison of the bifurcation diagram for the model with the data-based bifurcation diagram in Fig. 3 demonstrates that the model approximates the positions of the three equilibrium points and three bifurcation points very well. The average position and amplitude of the limit cycle oscillations differ between the two bifurcation diagrams, but these were not expected to be fully identical.

VI. CONCLUSION

The solution to a convection problem with a pressure source centered at the left boundary can be characterized by three state variables: the potential energy related to the pressure gradient, P, the fluctuation energy, N, and the zonal flow energy, F. Depending on the strength of the pressure source, q, we identified four different types of solutions to the convection problem. Three of these solution types corresponded to equilibrium points and the fourth type corresponded to a limit

cycle in the (P, N, F)-state space. Simulation data were generated for multiple fixed values of $q \in [0, 10]$ by computing and saving the three energy variables P, N, and F and their time derivatives at each output time step while solving the convection problem.

Purely based on the simulation data, we used SINDy[17] and some data fitting to identify a nonlinear dynamical system that models the time evolution of the three state variables. This approach revealed a predator-prey relationship between the zonal flow energy and the turbulent flow energy. We investigated the quality of the model by comparing positions of equilibrium points, bifurcation points, and solutions with the corresponding data from which the model was extracted. The model proved to be very accurate for each of these parameters.

We have demonstrated an approach to recovering reduced models for plasma dynamics, which serves as an alternative to the physical modeling approach. Further work could include identification of a reduced L–H transition model based on simulation data from a fluid model which is able to reproduce the L–H transition such as the HESEL model.[28,29] The same modeling approach could ultimately also be applied to derive models from experimental data. Even more accurate models might be obtained by replacing the SINDy algorithm with the more advanced implicit-SINDy algorithm[30] which extends SINDy to allow rational functions.

ACKNOWLEDGMENTS

M.D. thanks the people at the Mathematics Institute of Computational Science and Engineering, EPFL, for hospitality and useful discussions during a research stay where this paper was partly written.

[1]Ö. D. Gürcan and P. H. Diamond, J. Phys. A: Math. Theor. **48**, 293001 (2015).
[2]P. Morel, Ö. D. Gürcan, and V. Berionni, Plasma Phys. Controlled Fusion **56**, 015002 (2014).
[3]F. Wagner, Plasma Phys. Controlled Fusion **49**, B1 (2007).
[4]H. Sugama and W. Horton, Plasma Phys. Controlled Fusion **37**, 345 (1995).
[5]R. Ball, R. L. Dewar, and H. Sugama, Phys. Rev. E **66**, 066408 (2002).
[6]E.-J. Kim and P. H. Diamond, Phys. Plasmas **10**, 1698 (2003).
[7]R. Ball, Phys. Plasmas **12**, 090904 (2005).
[8]M. A. Malkov and P. H. Diamond, Phys. Plasmas **16**, 012504 (2009).
[9]H. Zhu, S. C. Chapman, and R. O. Dendy, Phys. Plasmas **20**, 042302 (2013).
[10]M. Dam, M. Brøns, J. Juul Rasmussen, V. Naulin, and G. S. Xu, Phys. Plasmas **20**, 102302 (2013).
[11]G. S. Xu, L. Shao, S. Liu, H. Wang, B. Wan, H. Guo, P. Diamond, G. Tynan, M. Xu, S. Zweben, V. Naulin, A. Nielsen, J. Juul Rasmussen, N. Fedorczak, P. Manz, K. Miki, N. Yan, R. Chen, B. Cao, L. Chen, L. Wang, W. Zhang, and X. Gong, Nucl. Fusion **54**, 013007 (2014).
[12]H. Zhu, S. C. Chapman, R. O. Dendy, and K. Itoh, Phys. Plasmas **21**, 062307 (2014).
[13]K. Miki, P. H. Diamond, Ö. D. Gürcan, G. R. Tynan, T. Estrada, L. Schmitz, and G. S. Xu, Phys. Plasmas **19**, 092306 (2012).
[14]X. Wu, G. S. Xu, B. Wan, J. Juul Rasmussen, V. Naulin, and A. H. Nielsen, Nucl. Fusion **55**, 053029 (2015).
[15]L. Ljung, *System Identification: Theory for the User*, 2nd ed., Prentice-Hall Information and System Sciences Series (Prentice Hall, 1999).
[16]S. Kobayashi, Ö. D. Gürcan, and P. H. Diamond, Phys. Plasmas **22**, 090702 (2015).
[17]S. L. Brunton, J. L. Proctor, and J. N. Kutz, Proc. Natl. Acad. Sci. U.S.A. **113**, 3932 (2016).
[18]W.-X. Wang, R. Yang, Y.-C. Lai, V. Kovanis, and C. Grebogi, Phys. Rev. Lett. **106**, 154101 (2011).
[19]N. Bian, S. Benkadda, O. E. Garcia, J.-V. Paulsen, and X. Garbet, Phys. Plasmas **10**, 1382 (2003).
[20]O. E. Garcia, N. H. Bian, J.-V. Paulsen, S. Benkadda, and K. Rypdal, Plasma Phys. Controlled Fusion **45**, 919 (2003).
[21]N. H. Bian and O. E. Garcia, Phys. Plasmas **12**, 042307 (2005).
[22]O. E. Garcia, N. H. Bian, V. Naulin, A. H. Nielsen, and J. Juul Rasmussen, Phys. Plasmas **12**, 090701 (2005).
[23]O. E. Garcia, N. H. Bian, and W. Fundamenski, Phys. Plasmas **13**, 082309 (2006).
[24]A. Getling, *Rayleigh-Bénard Convection - Structures and Dynamics*, Advanced Series in Nonlinear Dynamics (World Scientific Publishing, 1998), Vol. 11.
[25]O. E. Garcia, V. Naulin, A. H. Nielsen, and J. Juul Rasmussen, Phys. Plasmas **12**, 062309 (2005).
[26]O. E. Garcia, J. Horacek, R. A. Pitts, A. H. Nielsen, W. Fundamenski, J. P. Graves, V. Naulin, and J. Juul Rasmussen, Plasma Phys. Controlled Fusion **48**, L1 (2006).
[27]"COMSOL Multiphysics® v. 5.2a," COMSOL AB, Stockholm, Sweden.
[28]A. Nielsen, G. Xu, J. Madsen, V. Naulin, J. Juul Rasmussen, and B. Wan, Phys. Lett. A **379**, 3097 (2015).
[29]J. Juul Rasmussen, A. H. Nielsen, J. Madsen, V. Naulin, and G. S. Xu, Plasma Phys. Controlled Fusion **58**, 014031 (2016).
[30]N. M. Mangan, S. L. Brunton, J. L. Proctor, and J. N. Kutz, IEEE Trans. Mol. Biol. Multi-Scale Commun. **2**, 52 (2016).